



High-temperature thermal storage using a packed bed of rocks – Heat transfer analysis and experimental validation

Markus Hänchen^a, Sarah Brückner^b, Aldo Steinfeld^{a,b,*}

^a Solar Technology Laboratory, Paul Scherrer Institute, 5232 Villigen PSI, Switzerland

^b Department of Mechanical and Process Engineering, ETH Zurich, 8092 Zurich, Switzerland

ARTICLE INFO

Article history:

Received 15 April 2010

Accepted 7 October 2010

Available online 2 March 2011

Keywords:

Concentrated solar power

Thermal storage

Packed bed

Porous media

Sensible heat

ABSTRACT

High-temperature thermal storage in a packed bed of rocks is considered for air-based concentrated solar power plants. The unsteady 1D two-phase energy conservation equations are formulated for combined convection and conduction heat transfer, and solved numerically for charging/discharging cycles. Validation is accomplished in a pilot-scale experimental setup with a packed bed of crushed steatite (magnesium silicate rock) at 800 K. A parameter study of the packed bed dimensions, fluid flow rate, particle diameter, and solid phase material was carried out to evaluate the charging/discharging characteristics, daily cyclic operation, overall thermal efficiency and capacity ratio.

© 2011 Elsevier Ltd. All rights reserved.

1. Introduction

Concentrated solar power (CSP) technology, e.g., parabolic trough, tower, and dish systems, deliver high-temperature heat for driving Rankine (600–900 K), Brayton (1300–1600 K), and Stirling (~1000 K) heat-engine-based power plants. Because of the intermittency of solar radiation, 24-h dispatchability of electricity requires either fossil-fuel hybridization or thermal storage. The latter, in the form of sensible heat storage in a packed bed of rocks is especially suitable when air is used as the heat transfer fluid (HTF) in the solar receiver. The advantages are three-fold: 1) operating temperature constraints due to chemical instability of the HTF or the rocks are eliminated; 2) operating pressure can be close to ambient, avoiding the need for complex sealings; 3) the thermal storage can be incorporated directly after the receiver, eliminating the need for a heat exchanger between the HTF and the thermal storage medium. Further, by employing conventional materials of construction, significantly lower fabrication costs are expected than those for existing storage systems based on molten salts and steam. On the other hand, the disadvantages are associated with the larger air mass flow rates and surface area needed due to the lower volumetric heat capacity and thermal conductivity of air as

compared to those of thermo-oils, molten salts, sodium, or other heat transfer fluids proposed. These drawbacks translate into higher pressure drops and concomitant energy penalties. Energy densities for a concrete-based thermal storage system have been estimated at 22 kWh/m³, resulting in 50 000 m³ sized storage for a 50 MW parabolic trough power plant with 1100 MWh_{th} storage capacity [1].

As it will be shown in the analysis that follows, efficient thermal storage is accomplished through stratification [2] and effective heat transfer. Porous structures which maximize heat transfer between fluid and storage media and minimize heat transport inside the storage media fulfill both requirements. Stratification is also enhanced by a minimized cross-sectional area normal to the fluid flow direction. A wide body of publications describes numerical models for sensible heat storage in packed beds, but only a few include experimental validation, noteworthy among these are Coutier and Farber [3], Beasley and Clark [4], and Adebisi et al. [5]. Early literature focused on describing the transient behavior and expanding the range of operating conditions beyond those applicable to the analytical solution of the Schumann model [6] and the various numeric modeling approaches were compared by Ismail and Stuginsky [7]. Multiple studies have evaluated the second law efficiencies, thus accounting for the energy lost due to the effects of viscosity and other irreversibilities [8–11]. An aspect rather neglected so far is the behavior of a thermal storage over multiple charge and discharge cycles. For repetitive consecutive cycles, a cyclic steady state will manifest itself. This important effect was

* Corresponding author. Department of Mechanical and Process Engineering, ETH Zurich, 8092 Zurich, Switzerland. Tel.: +41 44 632 7929; fax: +41 44 632 1065. E-mail address: aldo.steinfeld@ethz.ch (A. Steinfeld).

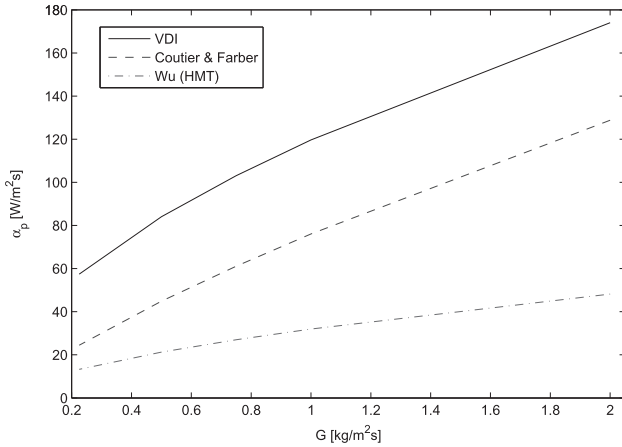


Fig. 1. Convective heat transfer coefficient as a function of the air mass flow rate per unit cross section, G . Plotted are the correlations by Coutier and Farber [3], VDI WärmAtlas [16], and Wu and Hwang [17].

studied in detail in only one recent publication [12], albeit for a generic application and using a model that had not been experimentally validated.

The present study presents a numerical heat transfer model of an air-based packed bed of rocks which is experimentally verified using previously published experimental results by this group [13]. The current model accounts for heat losses through the walls. It evaluates the thermal performance of charging and discharging cycles, including the energy cost associated with pumping work in a parametric study of the length of the packed bed, the fluid flow rate, the particle diameter, and the different solid phase material. Using an optimized design, the continuous 24-h operation of a thermal storage unit applied in a typical solar thermal power plant is simulated, providing the efficiency penalty such operation would entail.

2. Heat transfer analysis

The domain consists of the inside of a cylindrical tank, which is divided into a solid part, a packed bed of particles, and the fluid flowing through the void space surrounding the particles. A 1D two-phase transient model is formulated, which considers convection and conduction heat transfer, and assumes: 1) solid and fluid phases; 2) 1D Newtonian plug flow; 3) uniformly packed bed of constant solid heat capacity; 4) temperature gradient in radial direction is neglected; 5) uniform temperature particles, as justified by $Bi \leq 1$; 6) no internal heat generation; 7) no mass transfer; 8)

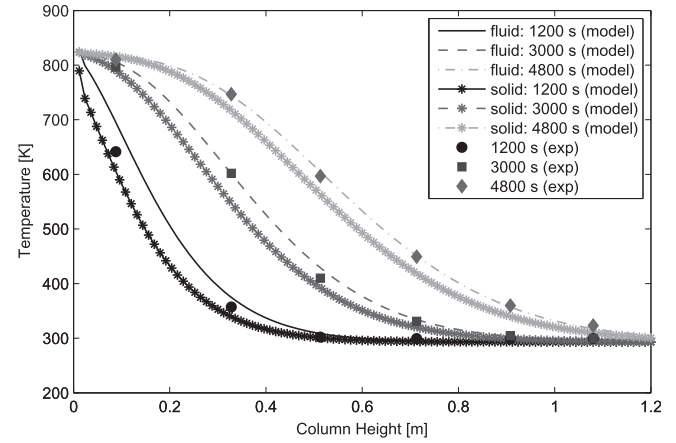


Fig. 2. Numerically modeled and experimentally measured temperature profiles across the pilot storage tank, after 1200, 3000 and 4800 s.

radiation heat transfer is neglected, as justified by the temperature level; 9) heat conduction in the fluid phase is neglected in the fluid phase energy balance, as it is small compared to the convective heat transfer. The governing unsteady energy conservation equations are:

For the fluid phase:

$$\frac{\partial T_a}{\partial t} + \frac{G}{\rho_a \varepsilon} \frac{\partial T_a}{\partial x} = \frac{h_v}{\rho_a c_a \varepsilon} (T_s - T_a) + \frac{UD\pi}{\rho_a c_a A \varepsilon} (T_{inf} - T_a) \quad (1)$$

For the solid phase:

$$\frac{\partial T_s}{\partial t} = \frac{h_v}{\rho_s c_s (1 - \varepsilon)} (T_a - T_s) + \frac{k_{s,eff}}{\rho_s c_s (1 - \varepsilon)} \frac{\partial^2 T}{\partial x^2} \quad (2)$$

The initial conditions for the single charge cycle are:

$$T_a(t = 0) = T_s(t = 0) = T_{inf} \quad (3)$$

The initial conditions for the discharge cycle and multiple cycles are:

$$T_a(t = 0) = T_a(t_{end}) \quad (4)$$

$$T_s(t = 0) = T_s(t_{end}) \quad (5)$$

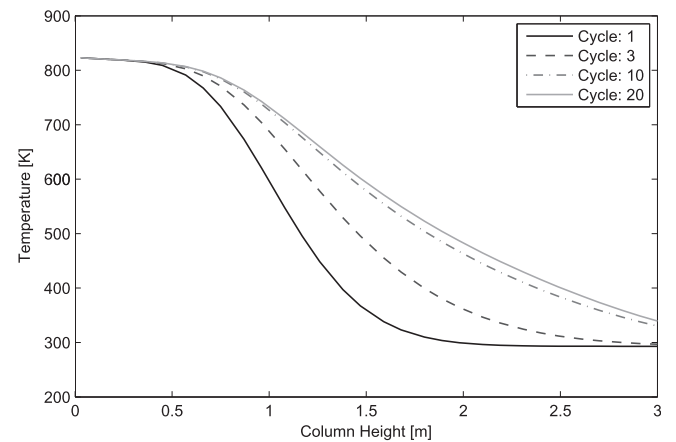


Fig. 3. Fluid temperature distribution across the storage height at the end of the charging period for a series of 6-h charge and 6-h discharge cycles. Baseline parameters: $H = 3$ m, $d = 0.02$ m, $G = 0.225$ kg/m² s, $T_{in} = 823$ K, solid material: steatite.

Table 1
Operational parameters of experimental setup.

Parameter	Value
T_{in}	823 K
T_{inf}	293 K
G	0.225 kg/m ² s
H	1.2 m
D	0.148 m
A	0.0172 m
ε	0.4
d	0.02 m
ρ_s	2680 kg/m ³
c_s	1068 J/(kg K)
k_s	2.5 W/(m K)
U	0.678 W/(m ² K)
n	100

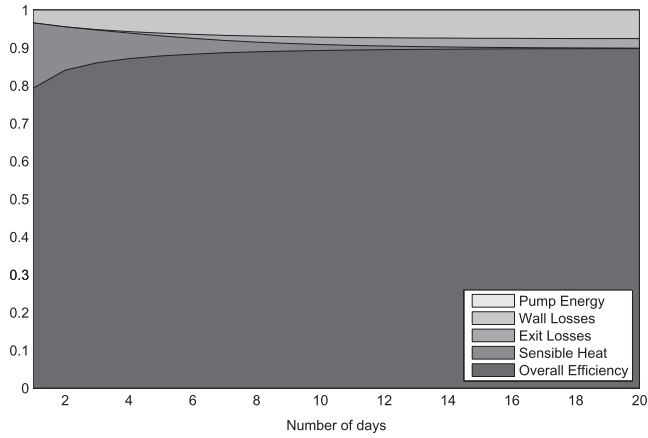


Fig. 4. Energy balance for cyclic operation over twenty days, with daily 6-h charge and 6-h discharge cycle. Baseline parameters: $H = 3$ m, $d = 0.02$ m, $G = 0.225$ kg/m² s, $T_{in} = 873$ K, solid material: steatite.

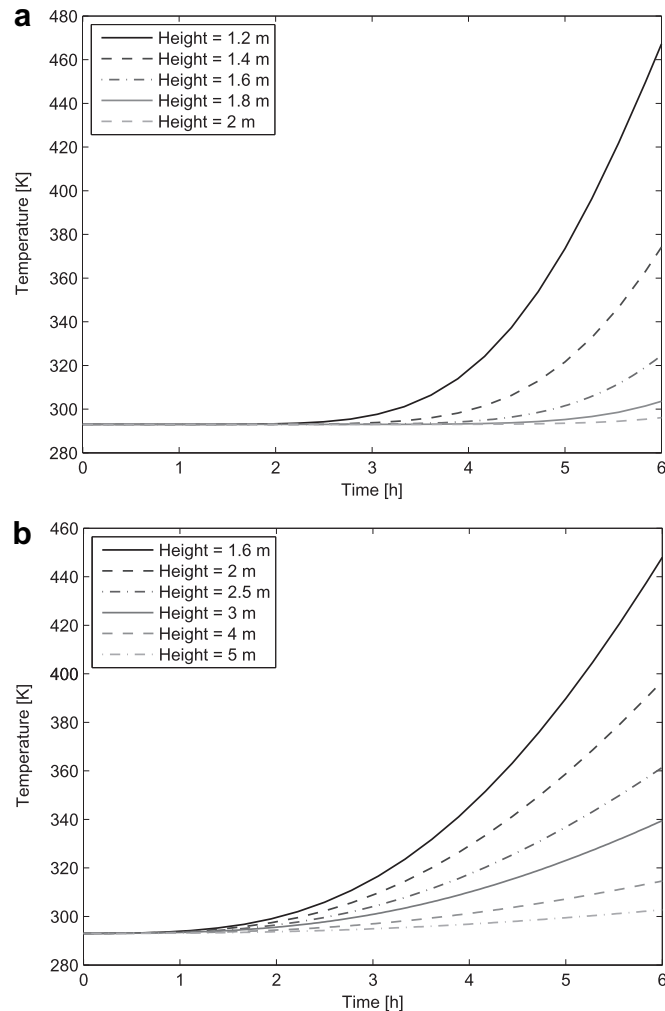


Fig. 5. Air temperature during the charging period as a function of time in the last layer for varying storage height. a: Single charge cycle. b: 20th cycle after a series of cycles.

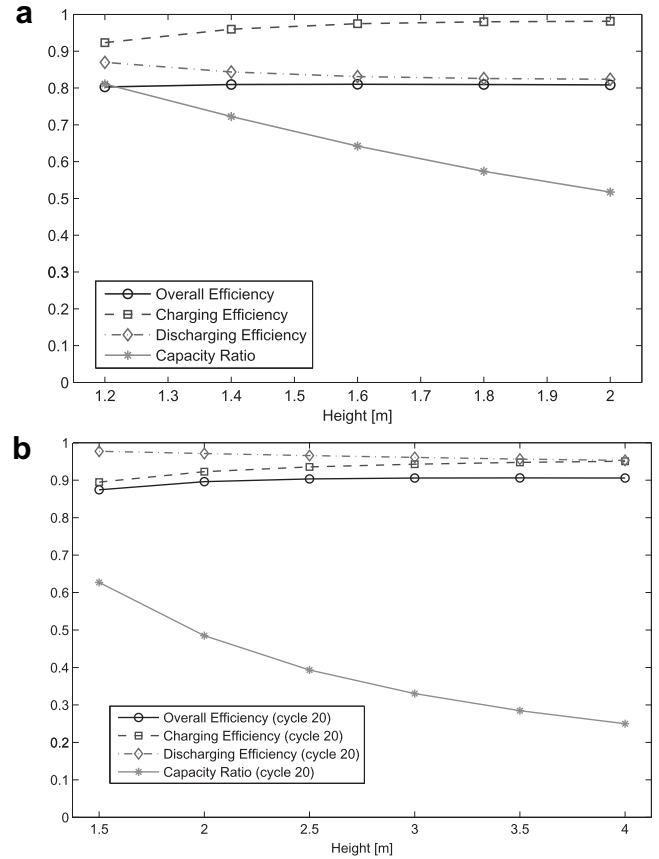


Fig. 6. Performance indicators as a function of the storage height. a: Single charge cycle. b: 20th cycle after a series of cycles.

i.e., the conditions at the end of the previous cycle. The boundary conditions are:

$$T_a(x = 0) = T_{in} \quad (6)$$

$$\frac{\partial T_a(x = H)}{\partial x} = 0 \quad (7)$$

$$\frac{\partial T_s(x = 0)}{\partial x} = \frac{\partial T_s(x = H)}{\partial x} = 0 \quad (8)$$

Eqs. (1) and (2) were discretized by applying the explicit-forward difference scheme in time and the upwind difference scheme in space. The pressure drop across the bed is given by [14,15]:

$$\Delta p = \frac{HG^2}{\rho d} \left(1.75 \frac{1-\varepsilon}{\varepsilon^3} + 150 \frac{(1-\varepsilon)}{\varepsilon^3} \frac{\mu}{Gd} \right) \quad (9)$$

which is valid for $1 \leq Re \leq 10^4$ and therefore suited for the present study. For the energy cost associated with this pressure drop, isothermal compression is assumed. Fig. 1 shows the heat transfer coefficient α_p between the air and the packed bed as a function of the air mass flow rate per unit cross section, G , calculated using Coutier and Farber [3]:

$$\alpha_p = \frac{700}{6(1-\varepsilon)} G^{0.76} d^{0.24} \quad (10)$$

Also plotted is α_p calculated using correlations by VDI WärmAtlas [16], and Wu and Hwang [17]. The volumetric heat transfer coefficient h_v is related to α_p via $h_v = 6(1-\varepsilon)/d \cdot \alpha_p$.

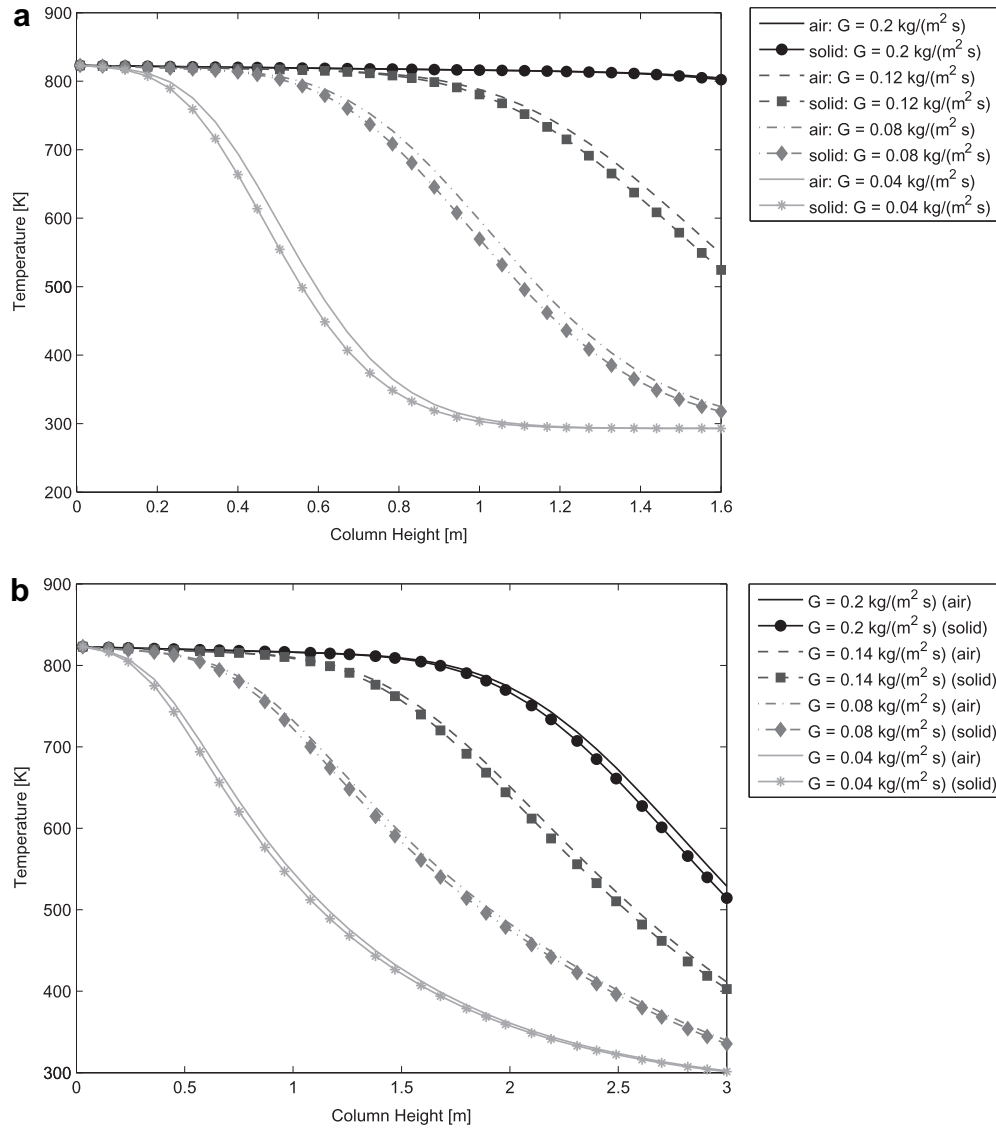


Fig. 7. Temperature distributions of the solid and fluid phases across the storage height at the end of the charging period for varying mass flow rate per unit cross section G , ranging from 0.04 to 0.2 kg/(m² s). a: Single charge cycle. b: 20th cycle after a series of cycles.

The effective thermal conductivity is given by [18,19]:

$$k_{s,eff} = [\varepsilon k_a^{-1} + (1 - \varepsilon) k_s^{-1}]^{-1} \quad (11)$$

$k_{s,eff}$ values compare well with those calculated with more complex models by Haussener et al. [20] and by Russell [21]. The overall heat loss coefficient through the wall is given by Incropera [22],

$$\frac{1}{U} = \frac{1}{\alpha_i} \frac{d_r}{D} + \frac{D}{2} \sum_{j=1}^n \frac{1}{\lambda_j} \ln \frac{d_{j+1}}{d_j} + \frac{1}{\alpha_{ao}} \frac{d_r}{d_{n+1}} \quad (12)$$

where radiation losses on the outside wall are neglected for simplicity as their contribution to the overall heat loss is estimated to be less than 5%. For α_{ao} , a correlation for natural convection on a free standing wall given by VDI Wärmeatlas [16] is applied:

$$\frac{\alpha_{ao} H}{k_{ao}} = Nu_{ao} = [0.825 + 0.387 [Ra \cdot f_1(Pr)]^{\frac{1}{6}}]^2 \quad (13)$$

$$f_1(Pr) = \left[1 + \left(\frac{0.492}{Pr} \right)^{\frac{9}{16}} \right]^{\frac{-16}{9}} \quad (14)$$

The convective heat transfer coefficient on the inside of the tank is given by [7,23]:

$$\alpha_i = \left(\frac{k_f}{d} \right) (2.58 Re^{\frac{1}{3}} + 0.094 Re^{0.8} Pr^{0.4}) \quad (15)$$

The density, heat capacity, thermal conductivity, and dynamic viscosity of air were calculated at an average temperature $T_{av} = (T_{in} + T_{inf})/2$ [16].

3. Experimental validation

The model was validated using experimental data published earlier by this group [13]. Measurements were made on a pilot tank built out of a vertically oriented packed bed of crushed steatite (magnesium silicate rock). Operational parameters are listed in

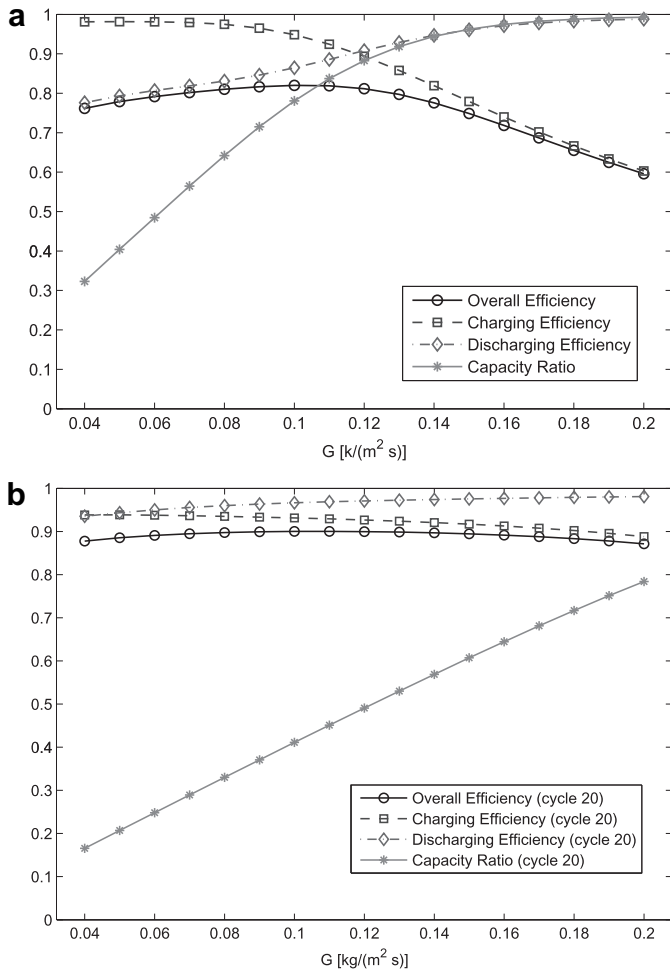


Fig. 8. Performance indicators as a function of the mass flow rate per unit cross section. a: Single charge cycle. b: 20th cycle after a series of cycles.

Table 1. The wall insulation comprises three different layers, with a calculated overall heat transfer coefficient $U = 0.678 \text{ W/(m}^2 \text{ K)}$ at 523 K.

Since $D/d = 7.4$, the plug flow assumption introduces inaccuracies because of wall effects, as higher velocities are developed in the low porosity areas next to the boundaries. This effect is only relevant for narrow tanks and can usually be neglected for $D/d \geq 40$ [13,16]. A bypass flow close to the wall has been introduced to account for this effect. As an approximation, it is assumed that the bypass flow (by-)passes the column without thermally interacting with the packed bed, thus the flow passing through the packed bed is reduced by a given amount.

The numerically modeled and experimentally measured gas temperature profiles across the pilot storage tank are shown in Fig. 2 after 1200, 3000, and 4800 s. Good agreement was achieved with a bypass flow rate equivalent to 15% of the total mass flow rate. The choice of α_p has a strong influence on the profile shape, and the selected correlation [3] provided a better match than others considered [24,25].

4. Continuous operation

A thermal storage unit is simulated for a series of consecutive 6-h charge and 6-h discharge daily cycles, as typical for a solar thermal power plant operation when extending the power

generation into the night. During the 12-h interval, the fluid flow is halted which stops forced convective heat transfer. As the hot end of the bed is situated at the top of the unit (stratification), natural convection is minimal during this period and is neglected along with wall losses for the 12-h halting interval. For the simplified case of identical charge and discharge profiles for a succession of days, the temperature profile inside the storage tank converges towards a cyclic steady state. Fig. 3 shows the fluid temperature distribution across the storage height at the end of the charging period for a series of 6-h charge and 6-h discharge cycles of 1, 3, 10 and 20 cycles. Baseline parameters used were $H = 3 \text{ m}$, $D = 0.8 \text{ m}$, $d = 0.02 \text{ m}$, $G = 0.225 \text{ kg/m}^2 \text{ s}$, $T_{in} = 823 \text{ K}$, solid material: steatite, corresponding to the parameters of the experimental tank except for a larger diameter and length. Compared to the temperature profile obtained when charging a tank initially at ambient temperature, the temperature profile flattens as it approaches the cyclic steady state.

The transient behavior while reaching the cyclic steady state is best illustrated using the overall energy balance:

$$1 = \frac{E_{outflow} + E_{wall} + E_{exit} + E_{sensible} + E_{pump}}{E_{input} + E_{pump}} \quad (16)$$

with the extracted energy during discharge, $E_{outflow}$, the losses through the wall, E_{wall} , the losses at the bed exit, E_{exit} , the energy needed to heat up the storage tank, $E_{sensible}$, the pump energy, E_{pump} , and the energy added during charging, E_{input} . Fig. 4 shows the energy balance for the first twenty days with daily 6-h charge

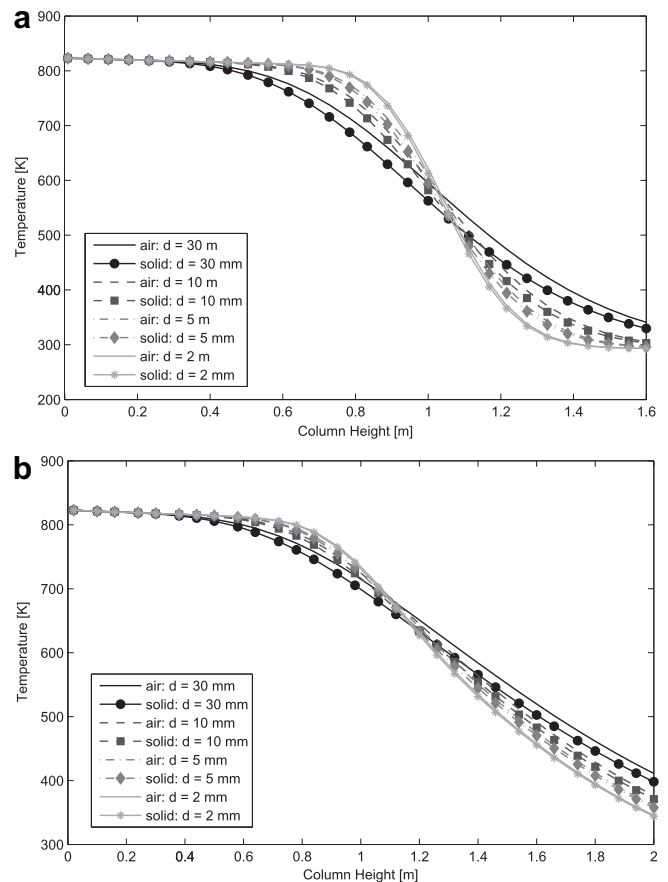


Fig. 9. Temperature distributions of the solid and fluid phases across the storage height for varying particle diameter at the end of the charging period. a: Single charge cycle. b: 20th cycle after a series of cycles.

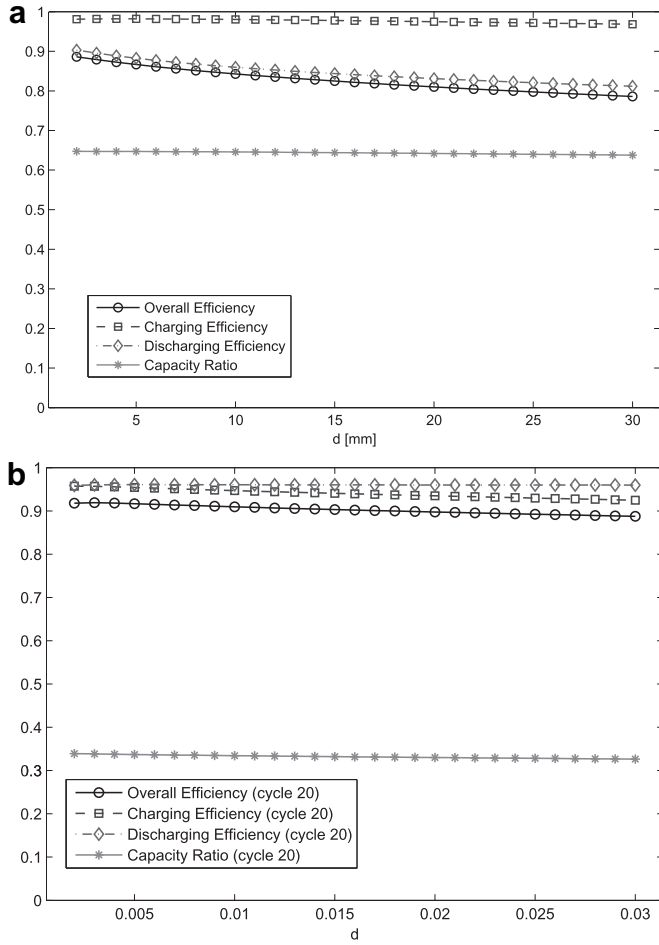


Fig. 10. Performance parameters as a function of the particle diameter. a: Single charge cycle. b: 20th cycle after a series of cycles.

and 6-h discharge cycles using the baseline parameters. Cyclic steady state is reached after about 20 cycles. Mainly during the first few cycles, the overall efficiency increases moderately as the amount of energy diverted to heat up the storage tank diminishes. Over time, the losses at the exit increase as the temperature front, as seen in Fig. 3, reaches the end of the column. The required pump energy is relatively small and not visible on the scale of the graph.

5. Parametric study

Two different scenarios are studied: 1) a tank, initially at ambient temperature, was charged for 6 h and then discharged for the same period of time and 2) a series of consecutive 6-h charge and 6-h discharge daily cycles, as described in the previous section.

For the baseline case, the dimensions of the pilot tank were modified in two aspects, all other parameters were retained. In order to be able to neglect wall effects, the tank diameter was increased to 0.8 m, achieving a $D/d = 40$ ratio. The storage length was increased to $H = 1.6$ m to increase the storage capacity for the single charge cycle and to $H = 3$ m for the continuous operation in order to make allowance for the flatter temperature profile observed after multiple cycles. The number of grid points was increased to $n = 200$ and 400, respectively.

Four performance indicators are defined that account for the change in the internal energy of the fluid entering and exiting the storage tank and of the solid heat storage media relative to

a reference state at $T_o = 293$ K and the pumping work of an isothermal compression. Energy stored in the heat transfer fluid itself is neglected as it constitutes a very small fraction of the stored energy. For the input and output flows, the change in the internal energy is thus:

$$E_{\text{input/output}} = \int_0^{t_{\text{end}}} \int_0^{T_a(t)} A \cdot G c_a dT dt \quad (17)$$

For the stored energy, integration is over the length of the storage tank:

$$E_{\text{stored}} = \int_0^L \rho_s c_s A (T_s(x) - T_o) dx \quad (18)$$

Placing the compressor before the solar receiver, the pumping work is carried out at ambient temperature and is given by:

$$E_{\text{pump}} = \int_0^{t_{\text{end}}} \frac{AG}{\rho_a} \Delta p dt \quad (19)$$

The charging efficiency is defined as:

$$\eta_{\text{charging}} = \frac{E_{\text{stored}}}{E_{\text{input}} + E_{\text{pump}}} \quad (20)$$

and describes the fraction of the input and pumping energy required to charge the storage tank. A low value of η_{charging} indicates ineffective heat transfer or energy lost by hot fluid leaving the tank, i.e., a tank charged with energy which can no longer be stored. The discharging efficiency is defined as:

$$\eta_{\text{discharging}} = \frac{E_{\text{outflow}}}{E_{\text{stored}} + E_{\text{pump}}} \quad (21)$$

and describes the ratio of the energy extracted from the storage tank relative to the energy stored and the pumping energy required for extraction. The overall efficiency is defined as:

$$\eta_{\text{overall}} = \frac{E_{\text{outflow}}}{E_{\text{input}} + E_{\text{pump(charging)}} + E_{\text{pump(discharging)}}} \quad (22)$$

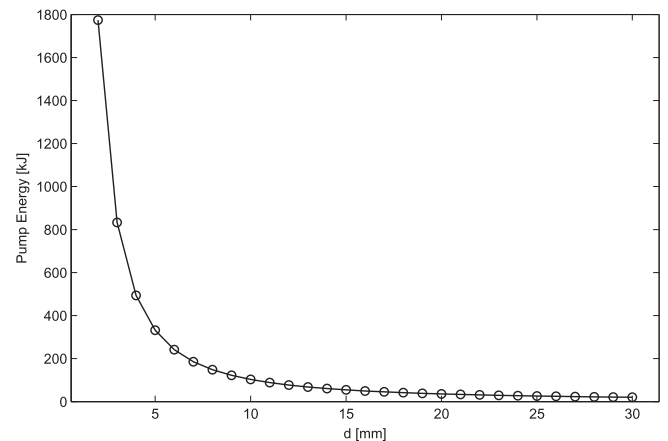


Fig. 11. Pumping energy as a function of the particle diameter for a single 6-h charge and 6-h discharge cycle.

Table 2
Alternative storage materials.

Material	Aluminum	Rock	Steatite	Steel
ρ_s (kg/m ³)	2700	2560	2680	7800
c_s (J/(kg K))	896	960	1068	571
c_{vs} (kJ/(m ³ K))	2419	2458	2862	4454
k_s (W/(m K))	204	0.48	2.5	50

and describes the ratio of the recovered energy for a single charge/discharge cycle to the input and pumping energy. The capacity ratio is defined as:

$$\sigma = \frac{E_{\text{stored}}}{E_{\text{max}}^{\text{stored}}} \quad (23)$$

and describes the amount of energy stored compared to the theoretical maximum energy that can be stored when the solid material in the tank reaches the input temperature of the air stream.

To evaluate a continuously operated storage unit over a series of consecutive 6-h charge and 6-h discharge daily cycles, the aforementioned performance indicators are redefined such as to use the end-state of the previous cycle as their base. To that effect, the stored cycle energy is defined as:

$$\hat{E}_{\text{stored}} = E_{\text{stored after charging}} - E_{\text{stored before charging}} \quad (24)$$

the amount of energy added to the store in a given charge cycle. The stored cycle energy, \hat{E}_{stored} , replaces E_{stored} in Eqs. (20), (21), and (23). The cycle charging efficiency is thus defined as:

$$\hat{\eta}_{\text{charging}} = \frac{\hat{E}_{\text{stored}}}{E_{\text{input}} + E_{\text{pump}}} \quad (25)$$

and describes the fraction of the input and pumping energy remaining as a net charge in the storage tank. The cycle discharging efficiency is defined as:

$$\hat{\eta}_{\text{discharging}} = \frac{\hat{E}_{\text{stored}}}{E_{\text{input}} + E_{\text{pump}}} \quad (26)$$

and describes the ratio of the energy extracted from the storage tank relative to the stored cycle energy and the pumping work required for extraction. The cycle capacity ratio is defined as:

$$\hat{\sigma} = \frac{E_{\text{stored}}}{E_{\text{max}}^{\text{stored}}} \quad (27)$$

and describes the net amount of newly stored energy for a given cycle compared to the theoretical maximal energy that can be stored were the solid material in the tank to reach the input temperature of the air stream. The definition of the overall efficiency remains unchanged. Only the values for the last, i.e., the 20th cycle are shown.

The influence of four parameters on the performance indicators was evaluated, namely: the storage height, the mass flow rate per unit cross section, the particle diameter, and the type of storage material.

5.1. Storage height

Fig. 5a and b shows the air temperature as a function of time in the last layer for different storage heights, varied in the range of 1.2–2.0 m, for a single charge cycle and in the range of 1.6–5 m for the 20th cycle after a series of cycles, respectively. The temperature of the air leaving the last layer increases by decreasing the storage

height from close to ambient temperature to more than 150 K above ambient temperature, leading to larger losses at the outlet. Fig. 6a and b shows the four performance indicators as function of the storage height. The most strongly affected indicator is the cycle capacity ratio which decreases markedly with increasing storage height. The overall efficiency rises slightly with increasing tank height as the losses by the hot fluid leaving the tank decrease with the lower fluid exit temperature associated with the longer tank length. The charging efficiency displays a modest increase with tank length due to lower losses at the tank exit. The discharging efficiency shows an opposite behavior with a modest decrease with tank height.

5.2. Mass flow rate

Fig. 7a and b shows the temperature distributions of the solid and fluid phases across the storage height at the end of a single 6-h charge cycle and the end of the charging period of the 20th cycle for different mass flow rates per unit cross section, G , varied in the range between 0.04 and 0.2 kg/(m² s). Higher flow rates lead to markedly higher temperatures at the bed exit, with the tank exit temperature almost reaching the inlet temperature for the maximum flow rate shown for the single charge cycle. Fig. 8a and b shows the variation of the performance indicators with the mass flow rate for a single 6-h charge and 6-h discharge cycle. Similarly to the variation of the storage height, changing the flow rate strongly affects the cycle capacity factor, which increases significantly with increasing flow rate. The charging efficiency, flat for low

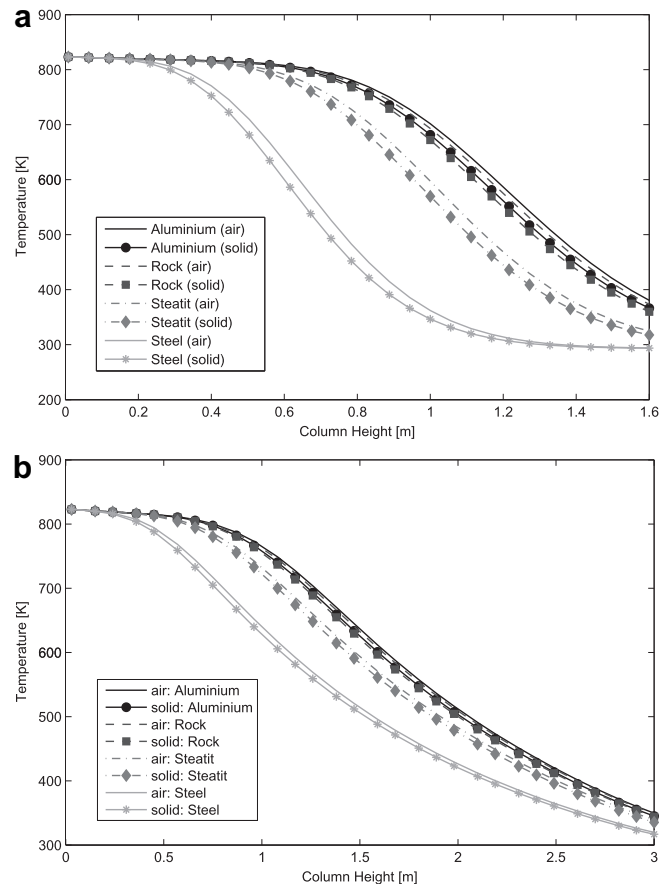


Fig. 12. Temperature distributions of the solid and fluid phases across the storage height at the end of the charging period for the four storage materials of Table 2. a: Single charge cycle. b: 20th cycle after a series of cycles.

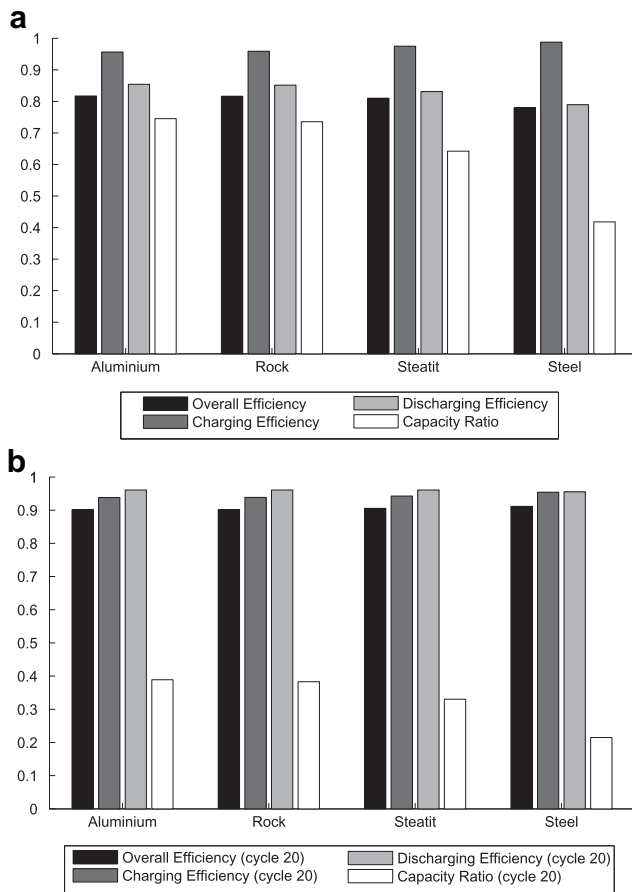


Fig. 13. Performance parameters for the four storage materials of Table 2. a: Single charge cycle. b: 20th cycle after a series of cycles.

flow rates, exhibits a steady decline for flow rates larger than $G = 0.08 \text{ kg}/(\text{m}^2 \text{ s})$, i.e., when the temperature front starts to reach the end of the column during the charge cycle. This effect is much less pronounced for the continuous operation. The overall efficiency shows a clear maximum in the lower half of the range of studied flow rates for the single charge and discharge cycle and a weak maximum in the middle of the range of the studied flow rates for the 20th cycle after a series of cycles.

5.3. Particle diameter

Fig. 9a and b shows the temperature distributions of the solid and fluid phases across the storage height at the end of a single 6-h charge cycle and the end of the charging period of the 20th cycle for different particle sizes, d , varied in the range between 2 and 30 mm. Smaller particle sizes lead to a steeper temperature profile, i.e., a narrower temperature front; this effect is smaller for the continuous operation. Moreover, the difference between the solid and fluid temperature noticeably narrows for smaller particles. This is a clear indication of an improved convective heat transfer between fluid and solid. Fig. 10a and b shows the variation of the performance indicators with the particle diameter. Both the discharging and the overall efficiency increase moderately with decreasing particle size, this effect is smaller for the continuous operation. The charging efficiency and the cycle capacity factor remain almost unchanged over the shown range of particle sizes. Fig. 11 shows the variation of the required pumping energy with the particle diameter for a single 6-h charge and 6-h discharge cycle.

The amount of pumping work increases significantly for small particle sizes. At a particle size of $d = 2 \text{ mm}$, the pumping work reaches almost 2% of the energy supplied to the tank. Nonetheless, is the maximum overall efficiency obtained for the smallest particle diameter, due to the sharper temperature front obtained with smaller particle sizes which allow for the more efficient extraction of the stored energy.

5.4. Storage material

Four different materials, namely: steatite, rock, aluminum, and 100Cr4 steel, are compared as storage material. In the scope of the simulation model, they differ in respect to heat capacity, thermal conductivity, and solid density. Table 2 shows the properties of the four materials considered, data taken from Aly and Elsharkawy [26]. Fig. 12a and b shows the temperature distributions of the solid and fluid phases across the storage height at the end of a single 6-h charge cycle and the end of the charging period of the 20th cycle for the four different materials of Table 2. The shape of the temperature fronts is similar for all four materials. It mainly differs in the axial position of the temperature gradient, with that for steel being the closest to the start of the column and that for aluminum and rock the furthest advanced into the bed. The relative position of the temperature front can be explained by the different volumetric heat capacities, $c_{v,s}$, of the four materials. The thermal conductivity, k_s , only has a minor influence as seen from the very similar temperature profiles of rock and aluminum, which differ significantly in their thermal conductivity but have similar volumetric heat capacities.

Fig. 13 shows the performance indicators for the four materials of Table 2. The four cases differ mainly in regard to the capacity ratio, which is notably lower for steel compared to the other three materials, indicating an under-utilization of the tank under the given conditions. Both rock and aluminum show slightly higher overall efficiencies than steatite and steel, as the size of tank as the operating conditions come closer to the optimum for those two materials. In practice, the choice of material should also consider thermal expansion, which is noticeably higher for metals than for most types of rock.

6. Conclusion

We have developed and experimentally validated a heat transfer model for a storage system consisting of a packed bed of rocks with air as the heat transfer fluid. A parametric study of the packed bed dimension, fluid mass flow rate, particle diameter, and solid phase material was carried out for evaluating the charging/discharging characteristics, daily cyclic operation, overall thermal efficiency and capacity ratio. For a continuous operation, the overall efficiency exceeds 90% under optimal conditions. A cyclic steady state is reached after about twenty 6-h charge and 6-h discharge daily cycles. The required pumping work remains, except for very small particle sizes, below 1% of the stored energy. The most relevant property of the storage material is the volumetric heat capacity, whereas the thermal conductivity of the solid only has a minor effect. For the range of particle sizes considered, the highest overall efficiency is found for the smallest particle size. High air mass flow rates and low storage heights and volumetric heat capacities of the solid material lead to superior capacity factor but to a reduction in the overall efficiency.

Acknowledgments

This study has been partially funded by the Swiss Federal Office of Energy.

Notation

A : area of bed cross section, m^2
 Bi : Biot-number $Bi = \alpha_p d / k_s$, –
 c_a : specific heat capacity of air, $J/(kg\ K)$
 c_s : specific heat capacity of the solid, $J/(kg\ K)$
 $c_{v,s}$: volumetric heat capacity of the solid, $kJ/(m^3\ K)$
 D : tank diameter, m
 d_r : reference diameter, m
 d : equivalent sphere diameter of solid particles, m
 d_j : diameter of insulation layer j , m
 E_{exit} : losses at the cold end of the tank during charging, J
 E_{input} : input energy, J
 $E_{outflow}$: energy extracted at the hot end of the tank, J
 E_{pump} : pumping energy, J
 $E_{sensible}$: net energy stored after a complete charge/discharge cycle, J
 E_{stored} : energy stored in the solid phase, J
 E_{stored} : additional energy stored per cycle in the solid phase, J
 E_{wall} : thermal losses through the outside wall of the tank, J
 g : standard gravity, $kg/(m\ s^2)$
 G : mass flow per unit cross section, $kg/(m^2\ s)$
 Gr : Grashof number $Gr = \beta k_s \Delta T g H^3 / \nu^2$, –
 H : height of the tank, m
 h_v : volumetric heat transfer coefficient between fluid and particle, $W/(m^3\ K)$
 k_a : thermal conductivity of air, $W/(m\ K)$
 k_{ao} : thermal conductivity of surrounding air, $W/(m\ K)$
 k_f : effective thermal conductivity of the fluid, $W/(m\ K)$
 k_j : thermal conductivity of insulation layer j , $W/(m\ K)$
 k_s : thermal conductivity of solid, $W/(m\ K)$
 $k_{s,eff}$: effective thermal conductivity of the packed bed, $W/(m\ K)$
 L : length/height of a layer, m
 n : number of grid points, –
 Nu_{ao} : Nusselt number of surrounding air, –
 Δp : pressure drop over the tank, Pa
 Pr : Prandtl number $Pr = c_a \mu k_f$, –
 Ra : Rayleigh number $Ra = Gr \cdot Pr$, –
 Re : Reynolds number $Re = Gd/\mu$, –
 t : time, s
 T_a : air temperature, K
 T_{av} : average air temperature, K
 T_{in} : inlet air temperature, K
 T_{inf} : ambient temperature, K
 T_o : reference temperature, K
 T_s : solid temperature, K
 U : overall heat transfer coefficient through the wall, $W/(m^2\ K)$
 V_{tank} : tank volume, m^3
 x : axial coordinate, m

Greek letters

α_{ao} : outer convective heat transfer coefficient, $W/(m^2\ K)$
 α_i : inner convective heat transfer coefficient, $W/(m^2\ K)$
 α_p : particle to fluid convective heat transfer coefficient, $W/(m^2\ K)$
 β : volumetric heat expansion coefficient of the fluid, $1/K$
 ε : void fraction, –
 $\eta_{charging}$: charging efficiency, –
 $\hat{\eta}_{charging}$: cycle charging efficiency, –

$\eta_{discharging}$: discharging efficiency, –
 $\hat{\eta}_{discharging}$: cycle discharging efficiency, –
 $\eta_{overall}$: overall efficiency, –
 ν_{ao} : kinematic viscosity of surrounding air, m^2/s
 μ : dynamic viscosity air, $Pa\ s$
 μ_{ao} : dynamic viscosity surrounding air, $Pa\ s$
 ρ_a : air density, kg/m^3
 ρ_s : solid density, kg/m^3
 σ : capacity ratio, –
 $\hat{\sigma}$: cycle capacity ratio, –

References

- [1] D. Laing, D. Lehmann, M. Fiss, C. Bahl, Test results of concrete thermal energy storage for parabolic trough power plants, *ASME J. Sol. Energ. Eng.* 131 (4) (2009) 041007.
- [2] D. Crandall, E. Thacher, Segmented thermal storage, *Sol. Energy* 77 (4) (2004) 435–440.
- [3] J. Coutier, E. Farber, Two applications of a numerical approach of heat-transfer process within rock beds, *Sol. Energy* 29 (6) (1982) 451–462.
- [4] D. Beasley, J. Clark, Transient-response of a packed-bed for thermal-energy storage, *Int. J. Heat Mass Transfer* 27 (9) (1984) 1659–1669.
- [5] G. Adebisi, E. Nsofor, W. Steele, A. Jalalzadeh-Azar, Parametric study on the operating efficiencies of a packed bed for high-temperature sensible heat storage, *ASME J. Sol. Energ. Eng.* 120 (1) (1998) 2–13.
- [6] T. Schumann, Heat transfer: a liquid flowing through a porous prism, *J. Franklin Inst.* 208 (1929) 405–416.
- [7] K. Ismail, R. Stuginsky, A parametric study on possible fixed bed models for pcm and sensible heat storage, *Appl. Therm. Eng.* 19 (7) (1999) 757–788.
- [8] R. Krane, A second law analysis of the optimum design and operation of thermal-energy storage-systems, *Int. J. Heat Mass Transfer* 30 (1) (1987) 43–57.
- [9] M. Taylor, R. Krane, J. Parsons, Second law optimization of a sensible heat thermal-energy storage-system with a distributed storage element. 1. Development of the analytical model, *ASME J. Sol. Energ. Eng.* 113 (1) (1991) 20–26.
- [10] M. Taylor, R. Krane, J. Parsons, Second law optimization of a sensible heat thermal-energy storage-system with a distributed storage element. 2. Presentation and interpretation of results, *ASME J. Sol. Energ. Eng.* 113 (1) (1991) 27–32.
- [11] J.J. Navarrete-Gonzalez, J.G.C. de Gortari, E. Torres-Reyes, Exergy analysis of a rock bed thermal storage system, *Int. J. Exergy* 5 (1) (2008) 18–30.
- [12] C. Singh, R.G. Tathgir, K. Muralidhar, Energy storage in fluid saturated porous media subjected to oscillatory flow, *Heat Mass Transfer* 45 (4) (2009) 427–441.
- [13] A. Meier, C. Winkler, D. Willemin, Experiment for modelling high temperature rock bed storage, *Sol. Energy Mater.* 24 (1991) 255–264.
- [14] S. Ergun, Fluid flow through packed columns, *Chem. Eng. Prog.* 48 (2) (1952) 89–94.
- [15] P. Chandra, D. Willits, Pressure-drop and heat-transfer characteristics of air-rockbed thermal storage-systems, *Sol. Energy* 27 (6) (1981) 547–553.
- [16] VDI-Wärmeatlas, tenth ed. Springer, Berlin, 2006.
- [17] C. Wu, G. Hwang, Flow and heat transfer characteristics inside packed and fluidized beds, *J. Heat Transfer-T ASME* 120 (3) (1998) 667–673.
- [18] A. Bejan, I. Dincer, S. Lorente, A.F. Miguel, A.H. Reis, Porous and Complex Flow Structures in Modern Technologies. Springer, New York, 2003.
- [19] A. Zbogor, F. Frandsen, P. Jensen, P. Glarborg, Heat transfer in ash deposits: a modelling tool-box, *Progr. Energ. Combust. Sci.* 31 (5–6) (2005) 371–421.
- [20] S. Haussener, P. Coray, W. Lipinski, P. Wyss, A. Steinfeld, Tomography-based heat and mass transfer characterization of reticulate porous ceramics for high-temperature processing, *J. Heat Transfer* 132 (023305) (2010) 1–9.
- [21] H. Russell, Principles of heat flow in porous insulators, *J. Am. Ceram. Soc.* 18 (1935) 1–5.
- [22] F.P. Incropera, Introduction to Heat Transfer, fifth ed. Wiley, Hoboken NJ, 2007.
- [23] J. Beek, Design of packed catalytic reactors, *Adv. Chem. Eng.* 3 (1962) 203–271.
- [24] G. Löf, R. Hawley, Unsteady-state heat transfer between air and loose solids, *Ind. Eng. Chem.* 40 (6) (1948) 1061–1070.
- [25] E. Alanis, L. Saravia, L. Rovetta, Measurement of rock pile heat-transfer coefficients, *Sol. Energy* 19 (5) (1977) 571–572.
- [26] S. Aly, A. Elsharkawy, Effect of storage medium on thermal-properties of packed-beds, *Heat Recov. Syst. CHP* 10 (5–6) (1990) 509–517.